AD-A059 715 PHYSICS INTERNATIONAL CO SAN LEANDRO CALIF F/G 20/8
INTENSE ELECTRON BEAM GENERATION AND COMPRESSION. ADVANCES IN H--ETC(U)
JAN 78 B ECKER, V BUCK, T S YOUNG, O LOPEZ DNA001-77-C-0167

UNCLASSIFIED PIFR-1045 DNA-4523F NL

2 OF 2
ADA
059715

END
DATE
FILMED
12-78
DDC

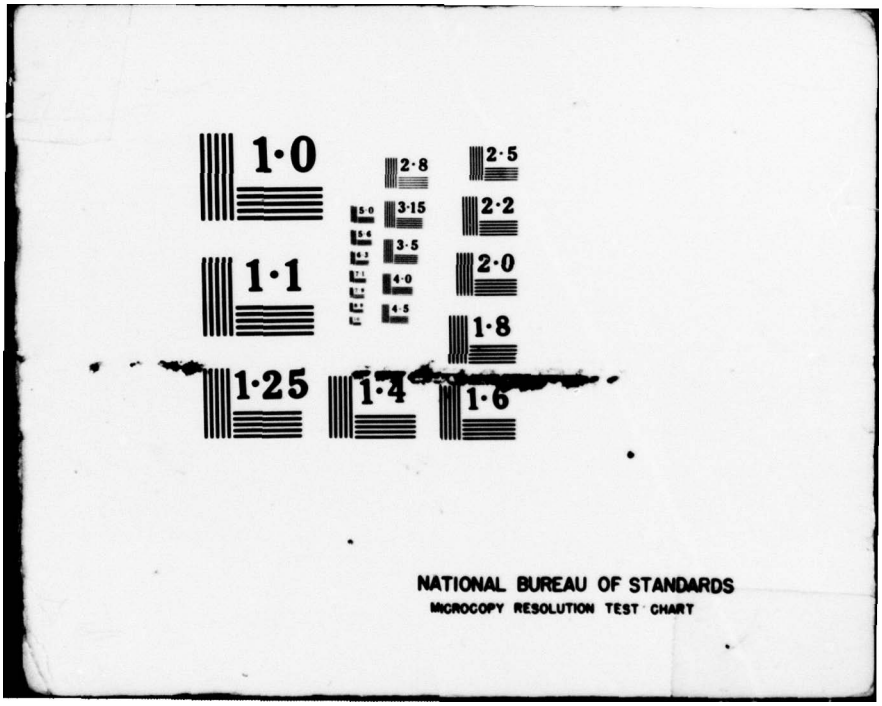
1·0
1·1
1·25
1·4
1·6
1·8
2·0
2·2
2·5
2·8
3·15
3·5
4·0
4·5
NATIONAL BUREAU OF STANDARDS
MICROCOPY RESOLUTION TEST CHART

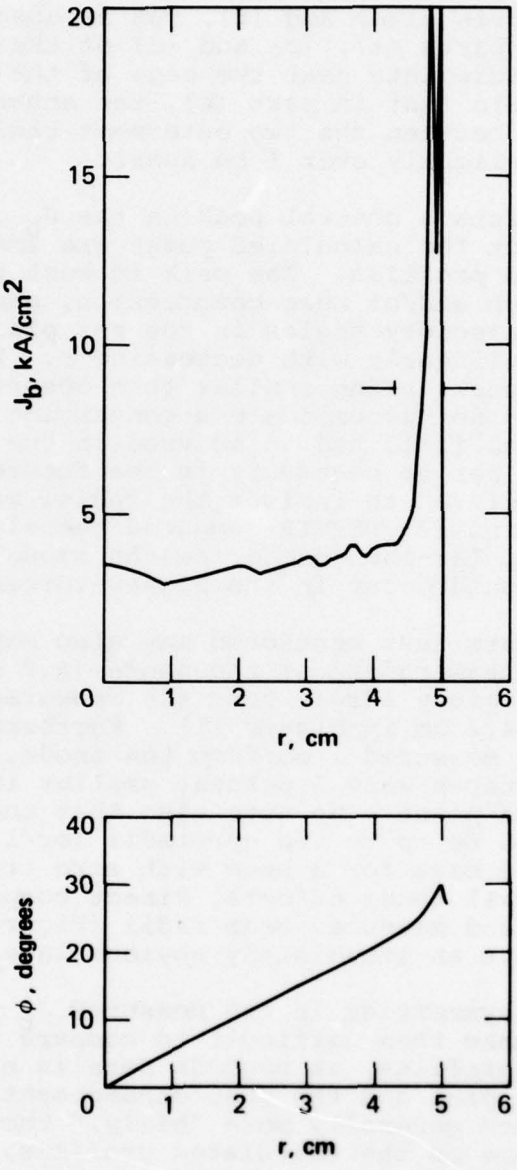

Figure 33 REEFER calculation of $J_b(r)$ and $\phi(r)$ at the anode, for 2.5 mm cathode dish depth and 10.0 mm A-K gap at V_d = 1.14 MV. As in Figure 32, J_b has been corrected for bipolar flow, whereas ϕ is from the monopolar calculation.

to comparison with the measured profiles, because of the current collectors' half-cm diameter. The effect is evident in Figures 11(e) and (f), but is absent in (b); the profiles in parts (a), (c) and (d) of the figure do not contain measurements near the edge of the beam. In fact it is possible that in part (b), the enhancement could have fallen between the two outermost radii of measurement, which were slightly over 1 cm apart.

- REEFER predicts a central peak in the J_b profile, as observed, but the calculated peaks are smaller than in the measured profiles. The peak is most probably caused by beam pinch and/or beam compression, and must occur if electron trajectory angles in the r-z plane go zero slower than linearly with decreasing r. Reasons for the calculated peaks being smaller than observed are (1) REEFER could not accommodate a converging guide field, so a paraxial field had to be used in the calculations (which will not be necessary in the future, as the code is to be modified to include the radial magnetic field component);and (2) REEFER computed the electron trajectories in the monopolar-mode diode, so the amount of pinching is less than would occur in the higher-current bipolar mode.

- The two points just mentioned may also explain why the calculated beam radius at the anode (4.9 cm in Figure 30) is non-negligibly larger than the measured beam radius (typically 4.2 cm in Figure 11). Furthermore, the $J_b(r)$ profile was measured 1 cm from the anode, where guide field flux tubes were 5 percent smaller in radius relative to the anode plane. We note also that the damage pattern radius could be up to two gyroradii (or 1 cm) larger than would be the case for a beam with zero transverse energy. Because of all these effects, direct comparison of the calculated and measured beam radii (Figures 11 and 30) does not have an immediately obvious interpretation.

- Azimuthal asymmetries in the measured J_b profiles in Figure 11 make them difficult to compare against the calculated profiles, as regards details of shape between the central peak and the edge enhancement. The measured profiles seem generally more "hilly," though of the same type of shape as the calculated profiles. Quantitatively, J_b amplitudes are in reasonable agreement in most cases; appreciable discrepancy occurs in the interior of the beam with the deeper-dished cathode, especially in Figure 11(e) at radii of about 1 and 2½ cm. Based on the measured J_b values at those locations, anode dose would have been marginally below the bipolar flow threshold (locally) at the time shown; the monopolar REEFER values of J_b do agree with the measurements. At larger radii (where the A-K was smaller by 2 to 2½ mm), anode dose should have been high enough to trigger bipolar flow by

the time shown. This case suggests that the cathode contour can be used to localize the region of bipolar flow. Referring again to Figure 11(e), the naturally-occurring central peak in the monopolar J_b profile must have been high enough to trigger bipolar flow at the axis.

- The theoretical $J_b \propto d^{-2}$ dependence of paraxial space-charge-limited flow between planar electrodes is evident in the REEFER results. The REEFER A-K gap at the axis was 11.15 mm for the 1.5 mm-deep cathode, and 12.5 mm for the 2.5 mm-deep cathode, giving a d^2 ratio of $(11.15/12.5)^2 = 0.796$. The calculated J_b values in the vicinity of the axis (averaged over the region $r < 1.5$ cm) are 3.2 kA/cm^2 and 3.9 kA/cm^2 for the 2.5 mm dish and 1.5 mm dish, respectively; $3.2/3.9 = 0.82$, in good agreement with the d^2 ratio.

- As calculated by REEFER, the electron angles at the anode plane are generally smaller than predicted by the net magnetic field-following model (Section 4). As an example, we consider the REEFER $\phi(r)$ results shown in Figure 32: at radii of 2.35 cm, 3.56 cm, and 4.9 cm, the field-following model* gives $\phi_{ff}/\phi = 1.28$, 1.30, and 1.66, respectively. The field-following model neglects the diode's axial electric field, which brings electron trajectories straighter toward the anode than would pure magnetic field-following motion. Furthermore, Figure 30 shows non-negligible radial components of electron velocity at the anode due to beam self-pinch. The effect of the radial velocity component is to increase ϕ; this effect (included in the $\phi(r)$ plot in Figures 32 and 33) also is neglected in the field-following model.

6.1.3 Limitations of REEFER. Several inadequacies were encountered in REEFER in the course of the studies just reported. Three points have already been mentioned: (1) numerical instability of regions with strongly non-uniform current density, such as pinched flow regions, due to coarse field-updating procedure; (2) inflexibility of electrode contouring due to a $\Delta r = \Delta z$ requirement in the code's Poisson-solving algorithm; (3) REEFER can not simulate bipolar flow or re-entrant electrons, which

*With $B_r = 0$, as in the REEFER calculation. Also, both ϕ_{ff} and the REEFER ϕ-values are from the monopolar flow case.

we have shown to be important features of diode behavior in the experimental domain of interest. To these points we add that REEFER is an equilibrium code, incapable of accounting for the effects of time-varying diode voltage on particle motion. This may not be a serious limitation for monopolar (electron) diodes, but could be important for bipolar diode simulation, because of relatively long ion transit times.

6.2 BEAM TRANSPORT AND COMPRESSION STUDIES USING THE COMPUTER CODE REFLEX

The computer code REFLEX was developed in this program to numerically evaluate the Young-Spence model of beam transport in a converging B_z guide field (Reference 3, reproduced in the appendix of this report). The model was originally motivated by current transport efficiency measurements (see Reference 3) which were higher than could be explained by calculations of simple adiabatic motion of beam electrons. The adiabatic calculations predicted too much mirroring (reflection) of electrons in the spatially increasing field. The Young-Spence model invoked electron axial reflexing between the B_z mirror (or lens) field and the cathode. Reflexing causes untransmitted electrons to repeatedly re-encounter the anode, where scattering produces a non-adiabatic change in pitch angle. If an electron's new angle is below the "loss-cone" angle $\sin^{-1}(M^{-\frac{1}{2}})$, where M is the ratio of peak B_z to B_z at the anode, the electron will then propagate through the lens. In our case, the loss-cone angle was 33 degrees. Since a radial "walk" accompanies scattering, an electron can leave the system (radially) before scattering puts its angle below the critical value for transmission. The Young-Spence model computes transport efficiency through the lens as the outcome of these two competing effects.

A detailed numerical treatment of the model was desirable because its analytic version (Reference 3) cannot take account of the variation of injected electron energy with time or the variation of injected beam current density with radius. Furthermore, the analytic model computes only charge transport efficiency, and unlike the new REFLEX code, cannot calculate other important features of the transmitted beam, such as total current versus time, current density profile versus time, and radius- and time-resolved energy and angle distributions. These transmitted beam quantities will be important as input data for Monte Carlo code computations of the energy deposition profile. Present emphasis is on refining the physics of the code based on experimental feedback.

As mentioned in the Introduction (Section 1), it initially seemed desirable to couple the transport code to REEFER, i.e., to use REEFER diode calculations as input to the transport calculation. The software for interfacing the two codes was in fact developed, but never used, because the injected electron angles computed by REEFER were for the monopolar flow mode and so were unrealistically low as it turned out. With the converging guide-field geometry, realistic electron angles of injection were felt to be essential for a meaningful test of the transport code. We therefore employed the field-following model as the best way of estimating angles of injection; this simple model was found to be consistent with angles measured near the anode (Section 4). The injected beam was also taken to have uniform current density, a reasonable approximation of the data [Figure 11(a) and (b)] for the purpose of initial tests of the code.

The new code, REFLEX, is phenomenological in nature. It segments the injected beam in radius and time and then tracks the evolving transport status of each beam segment according to analytic laws governing electron motion and scattering (diffusion). The output beam is fully described as a time-varying electron distribution over radius, energy, and angle. Certain adjustable parameters must be specified: (a) the radius at the anode, outside of which electrons are assumed to be lost from the system; (b) the scattering angle probability function describing the effect of each encounter with the anode foil and the intra-diode fields. The complex structure of the latter has prevented analytic calculation of the scattering distribution, so the code assumes re-injection with angles uniformly distributed up to a maximum angle which depends on electron energy and incident angle. Item (a), the containment radius at the anode can be identified experimentally in two ways. For the present study, it was determined by tracing back the guide-field flux tube at the edge of the compressed-beam damage pattern. The other way would be to place various plates with apertures of different diameters against the downstream side of the anode, in turn (with each plate thick enough to absorb incident electrons). The containment radius would be defined by the smallest aperture which does not affect beam transport.

6.2.1 REFLEX Calculations Compared with Experimental Results. The waveforms of injected electron current and energy that were used as inputs to the REFLEX calculations were the diode waveforms of Pulse 4048 (Figure 4b). As already described, the injected radial current profile was assumed uniform, with electron angles given by the field-following model in the diode. The target plane for which beam transport was calculated was taken to be the focal plane of 3:1 B_z lens, with the same field strength at the anode as in our experiments; the anode was also as in the experiments (½-mil titanium). Because the guide field is not subject to radial

dilation in the code (as evidently it was experimentally) the calculated transport efficiency and radial current profile shape are independent of target position at all points downstream from the focal plane. Experimentally, the lens ratio was 3.3:1 before beam injection, with the target (for compressed beams) at the 3:1 position, 5 cm downstream from the lens plane. We assume in the code that lens dilation during the pulse reduced the field upstream from the target, so that the actual field during beam transport increased monotonically from anode to target, where line-tying maintained the 3:1 value.

Figures 34 through 37 present REFLEX calculations of the transported and compressed beam. The figures show total current transport, total energy transport, radial current profile, and mean electron angle. (Other information which the code can provide, such as radius- and time-resolved electron angle and energy distributions in the transported beam, were not available in time for inclusion in this report.)

The ratio of the time-integrals of the current waveforms in Figure 34 gives a calculated charge transport efficiency of 80 percent, as compared with the experimental value of 95 percent (see Section 2). Total energy transport, in Figure 35, is calculated at 71 percent, as compared with an estimated 86 percent experimentally (based on the measured charge transport, as described in Section 2). The calculated transport values are about 83 percent of the experimental values. This modest but non-negligible discrepancy indicates a need for further refinement of the code's modeling of non-adiabatic scattering when reflexing electrons reencounter the anode and the diode fields. It is encouraging that the transported current waveform in Figure 34 exhibits the same qualitative behavior, relative to the injected current, as does the experimental waveform (Figure 5a in Section 2): very high

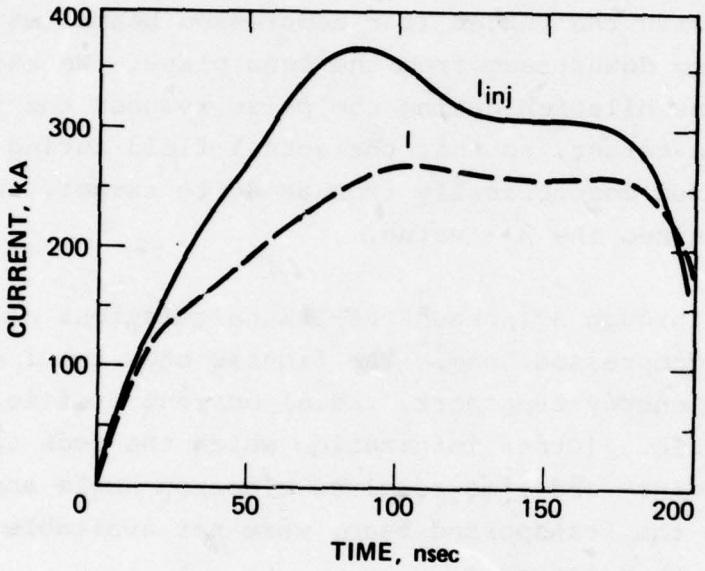

Figure 34 REFLEX current transport calculation through 3:1 lens. Injected electron beam current (I_{inj}) and transported current (I) versus time. Total charge transport efficiency is 80 percent.

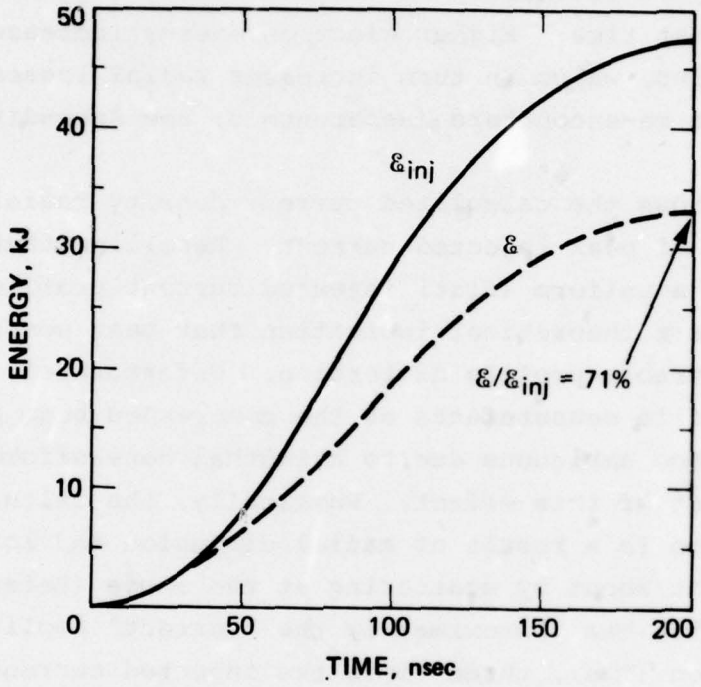

Figure 35 REFLEX energy transport calculation through 3:1 lens. Cumulative injected beam energy ($\&_{inj}$) and transported beam energy (&) versus time. Final transport efficiency is 71 percent.

current transport efficiency for the first 20 ns, followed by 85 ns of reduced efficiency, followed by higher efficiency for the rest of the pulse. The physical reason for the middle period of reduced transport efficiency is the relatively high diode voltage during that time. Higher electron energy increases the electron gyroradius, which in turn increases radial losses associated with anode re-encounters (Reference 3; see Appendix).

Figure 36 shows the calculated current density radial profile at the time of peak injected current. Recalling that the calculation used a uniform (flat) injected current profile, the figure represents a theoretical indication that beam compression may cause considerable profile distortion. Unfortunately, the experimental profile measurements at the compressed beam position (Section 3) are too ambiguous due to azimuthal non-uniformities to serve as a test of this effect. Physically, the calculated profile distortion is a result of radial diffusion and loss of electrons, brought about by scattering at the anode (Reference 3). The altered profile has approximately the "correct" amplitude in its central region (i.e., three times the injected current density, corresponding to factor-of-three area compression), but is deficient in the outer portion of the beam, because radial escape occurs from the beam surface.

The average electron angle plotted versus time in Figure 37 is the simple statistical instantaneous mean value. Different angle distributions can have the same mean value, so the latter is not the same as the instantaneous effective angle for electron energy or charge deposition in a target material. Therefore, the mean angle in Figure 37 should not be simply compared with the measured effective angles in Section 4 (Figure 19). Qualitatively, the time dependence of the average angle in Figure 37 differs from that of the effective angles in Figure 19, in that

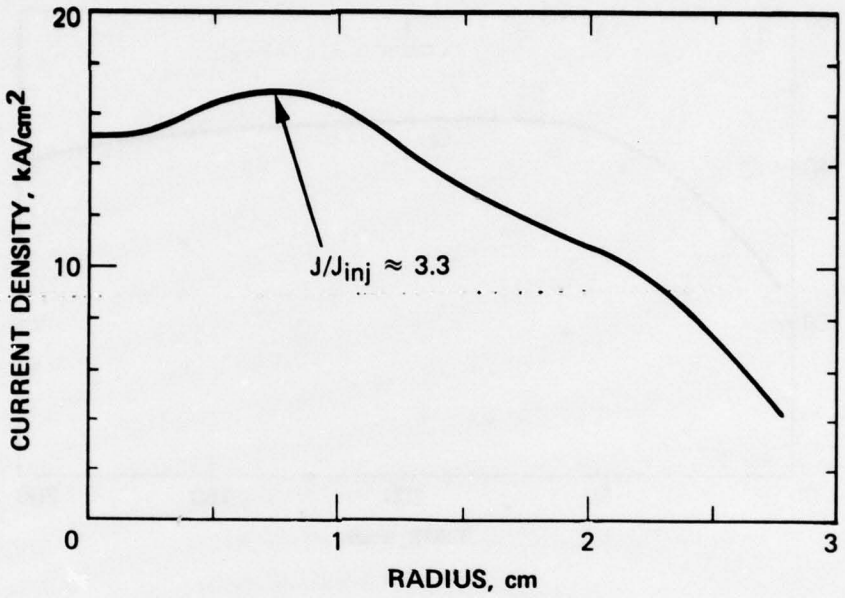

Figure 36 REFLEX calculation of compressed current density profile (J) at the target with 2.9:1 lens ratio, at the time of peak injected current. Maximum J is approximately 3.3 times the injected (uniform-profile) value.

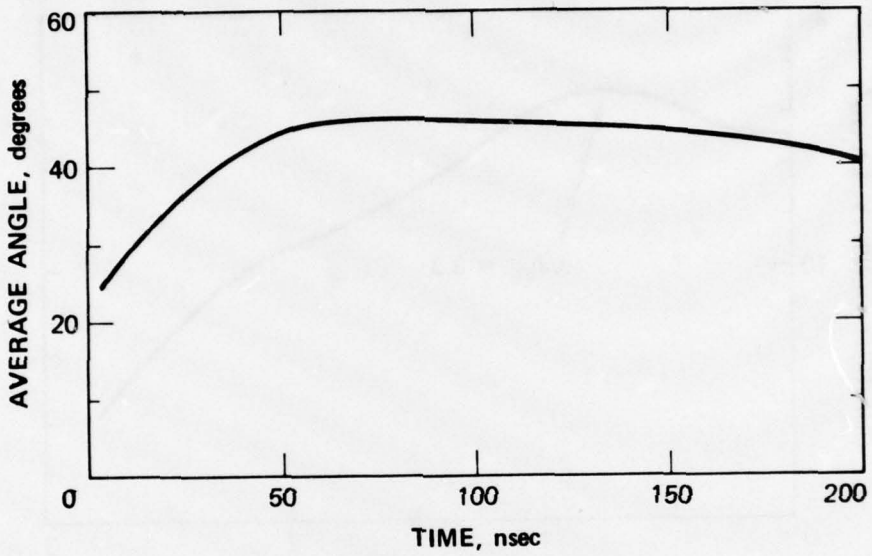

Figure 37 REFLEX calculation of average angle in 3:1 compressed beam versus time.

the latter decrease markedly as diode voltage falls toward the end of the pulse, whereas the calculated average angle does not. This discrepancy might indicate inaccuracies in the field-following model of diode electron angles, which was used to numerically generate the injected electron angles for REFLEX. The compressed-beam electron angle calculation would best be tested against the data by using the full calculated angle distribution as input for a Monte Carlo code computation of the beam current transmission profile. This computed profile could then be compared directly with filtered Faraday cup data.

SECTION 7

SUMMARY AND RECOMMENDATIONS

The main achievements, observations and conclusions of the Electron Beam Diagnostics Program can be summarized as follows:

1. The instantaneous cross-sectional profile of beam current density has been measured in 350 kA, 1.2 MV, 50 kJ beams, both near the anode and after factor-of-three area compression. The application of these measurements to high-dose calorimetry has been demonstrated.

2. Near the anode, the current density profile data are in general agreement with simulations performed using the REEFER diode code, provided the simulation results are adjusted according to bipolar flow theory. Experimental beam non-uniformities made it impossible to rigorously test the simulation.

3. The quantitative accuracy of filtered Faraday cup measurements of charge deposition profile has been established, and filtered Faraday cup data has been analyzed to give the first time-resolved measurements of electron angles in intense e-beams. This capability allows the accurate measurement of high-dose energy deposition profiles in samples of practical interest.

4. Beam compression by a factor of 3 in area was accomplished at ~ 95 percent charge transport efficiency and ~ 85 percent energy transport efficiency, giving peak dose of about 4000 cal/gm in carbon targets.

5. A new computer code, REFLEX, has been developed to numerically simulate the Young-Spence model of beam transport and compression in axial magnetic guide fields. REFLEX calculations of compressed-beam transport efficiency are about 17 percent less than measured values, suggesting a need for more detailed modeling of electron scattering in diode re-encounters.

6. Modification of diode behavior due to reflected electrons has been experimentally demonstrated, documenting the need to treat this effect in diode simulation codes.

Based on this program's findings, and in view of the overall program goal described in the Introduction, we recommend continuing efforts in the following areas:

7.1 EXPERIMENTAL

- Electrode surface treatment tests, aimed at subduing diode impedance collapse mechanism(s) in order to achieve beam azimuthal uniformity, detailed control of the radial current profile shape, and reproducibly full-duration, full-energy pulses.
- Compressed beam transport studies (such as lens ratio, anode thickness, and cathode contour variations) aimed at further revealing the mechanisms controlling beam transport.
- Radius-resolved measurements of charge deposition profile and electron angle by the filtered Faraday cup technique.
- Experimental studies to define the domain of validity of the single-angle beam model.

7.2 THEORETICAL/CALCULATIONAL

- Diode simulation development, including the effects of bipolar flow, re-entrant electrons, spatially varying guide field, and time-varying voltage.
- Transport theory studies, aimed at identifying the mechanism(s) which give measured transport efficiency in excess of presently predicted value.
- Monte Carlo code re-organization, to include time-varying electron angle.
- Calculations to identify single-angle beam model range of validity to complement/support experimental study.
- Calculational study of requirements for energy deposition profile radial uniformity (angle/fluence/dose/profile shape trade-off).

REFERENCES

1. K. Childers and J. Shea, "A Faraday Cup with Multiple Internal Filters and a Primary Current Monitor for Characterizing High Dose Pulsed Electron Beams," PIFR-835, Physics International Company, San Leandro, CA, October (1976); also available as Air Force Weapons Laboratory Report No. AFWL-TR-76-132 October (1976).

2. J. E. Boers, "Digital Computer Simulation of High-Current, Relativistic, and Field Emission Electron Tubes," 11th Symposium on Electron, Ion and Laser Beam Technology, R. M. Thornley, ed.; San Francisco Press, Inc., San Francisco, CA.

3. T. S. T. Young and P. Spence, "Model of Magnetic Compression of Relativistic Electron Beams," Appl. Phys. Letters, 29, 464-466 (1976).

4. D. Prono, J. Shearer and R. Briggs, Phys. Rev. Letters 37, 21 (1976); S. J. Stephanakis, D. Mosher, G. Cooperstein, J. Boller, and J. Goldon, Phys. Rev. Letters 37, 1543 (1976).

5. D. W. Forster, "High Current Electron Beam Acceleration in the Presence of an External Magnetic Field: Field Magnitude Criteria," Advanced Weapons Research Establishment report No. SSWA/DWF/742/648 February (1974).

6. D. Pellinen, Rev. Sci. Instr. 43, 1654 (1972).

7. R. D. Genuario and V. L. Bailey, "Characterization of Electron and Ion Current Flow in Very Large Aspect Ratio Terawatt Diodes," PIIR-7-77, Physics International Company, San Leandro, CA., November (1977).

8. M. J. Berger, "Monte Carlo Calculation of the Penetration and Diffusion of Fast Charged Particles," in Methods in Computational Physics, Vol. 1, ed., B. Alder, S. Fernbach and M. Rotenberg, Academic Press, N.Y. (1963).

9. K. Childers and J. Shea, "Material Response Technology on the Physics International Mylar Line," PIFR-423-1, Physics International Co., San Leandro, CA (1974); DNA 3448F (1975).

10. D. Prono, B. Ecker, N. Bergstrom and J. Benford, Phys. Rev. Letters 35, 438 (1975).

11. D. Prono, J. Creedon, I. Smith, and N. Bergstrom, J. Appl. Phys. 46, 3310 (1975).

12. M. Di Capua, R. Huff, and J. Creedon, "Experimental Investigations of Positive Ion Flow in a Double Diode," in Proceedings of the International Topical Conference on Electron Beam Research and Technology, G. Yonas, ed. (Sandia Laboratories report No. SAND76-5122), November (1975).

13. S. Langmuir, Phys. Rev. 33, 954 (1929); J. W. Poukey, Appl. Phys. Letters, 26, 145 (1975).

APPENDIX

MODEL OF MAGNETIC COMPRESSION OF RELATIVISTIC ELECTRON BEAMS

Model of magnetic compression of relativistic electron beams

T. S. T. Young and P. Spence

Physics International Company, San Leandro, California 94577
(Received 30 June 1976)

A theoretical model for the magnetic compression of relativistic electron beams is described. Calculations of the beam fraction transmitted through the magnetic mirror are in agreement with several experiments covering a broad parameter range.

PACS numbers: 84.80.Dz, 52.40.Mj

There have been several experimental studies on the compression of relativistic electron beams in low-pressure gas using externally imposed fields. At Sandia Laboratories,[1] magnetic compression up to mirror ratios in excess of 6:1 of a low ν/γ beam agreed with the adiabatic prediction that the beam should conserve its magnetic moment while propagating along the field lines. The transmitted beam fraction through the mirror was simply the beam population in the magnetic loss cone. At Cornell University, Davitian and Nation[2] obtained rather high transmitted beam fractions at mirror ratios of 3:1. In addition they found the compression of the beam cross-sectional area to be inversely proportional to the mirror ratio M, indicating that the beam electrons were tied to the vacuum field lines. In experiments with high ν/γ beams at Physics International Company,[3,4] transmission fractions were repeatedly observed to be much higher than the adiabatic prediction while the beam cross-sectional area appeared to scale as M^{-1}. Therefore, a theory is needed to explain the discrepancy among the various experiments in that the adiabatic theory accounts for the beam transmission in some experiments but is inadequate for the others.

It is proposed here that the beam electrons which are adiabatically reflected at the magnetic mirror can be trapped between the mirror and the electric potential at the cathode. The trapped electrons nonadiabatically change their pitch angles as well as their guiding flux tubes when passing through the anode. Hence, some fraction of the trapped electrons can eventually be transmitted through the mirror due to the nonadiabatic change of their pitch angles, while the remainder escape radially due to the random changes of their guiding centers. Beam transmission is enhanced over the simple adiabatic (single-pass) prediction when the radial escape rate is slow compared with the pitch angle scattering. The criterion for the transmission enhancement to occur is found to be

$$\rho_0/\sqrt{2}\,r_b(1-\cos\theta_c)^{1/2}<1, \tag{1}$$

where r_b is the beam radius at the anode in centimeters, θ_c is the loss cone angle, and ρ_0 (cm) $= 1.7(\gamma^2-1)^{1/2}/B_z$ (kG) is the full beam gyroradius in the plasma channel.

We assume that an electron beam with uniform density, which is generated in a vacuum diode, propagates in an axial magnetic guiding field and is compressed in a mirror field at the end of the transport region. The field is assumed to be strong enough to prevent beam pinching in the diode,[5] i.e.,

$$B_z\ (\mathrm{kG}) \geq 0.1\, I_b\ (\mathrm{kA})\ \gamma/d\ (\mathrm{cm})\ \nu. \tag{2}$$

In Eq. (2), I_b is the beam current, d is the cathode-anode distance, and ν/γ is the usual Budker parameter. In the transport and compression region, we assume that the beam is fully current neutralized and that the beam electrons are adiabatically guided by the vacuum field ($B = B_z\hat{z}$ just beyond the anode and $|B| = MB_z > B_z$ at the mirror). Diamagnetic effects are assumed unimportant because in most of the experiments[1-4] the beam cross sections appear to compress adiabatically. The configuration of the beam environment is schematically plotted in Fig. 1 for illustration.

In the diode, the uniform beam produces an azimuthal magnetic field, $B_\theta\hat{\theta}$, which adds vectorially to the applied axial B_z. For the cases where the diode electric field is small compared with the total B field, beam electrons are accelerated by the electric field along the total B field and, at the same time, gain a small $\mathbf{E}\times\mathbf{B}$ drift in the radial direction. The electrons then encounter the anode foil across which the spiral diode B field changes into the axial B_z. Assuming that the transition sheath at the anode foil is much thinner than a beam gyroradius, the beam electrons streaming across the anode sheath into the plasma channel obtain a pitch angle θ_r with respect to B_z, where

$$\theta_r = (r/r_b)\tan^{-1}(0.2\, I_b/r_b B_z) \equiv \theta_b r/r_b. \tag{3}$$

Scattering in the thin anode foil induces an additional pitch-angle spreading centered about the pitch angle θ_r, and the corresponding energy absorption is negligible. The angular spreading θ_s (which is a function of r

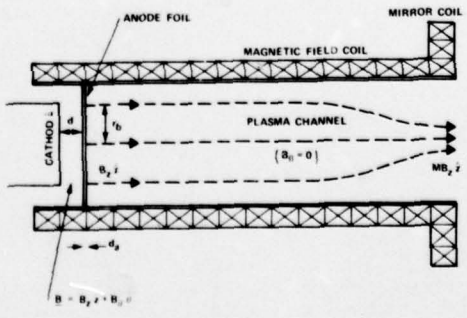

FIG. 1. Schematic configuration of the diode, beam transport, and beam compression regions.

because the beam incident angle θ_r and hence the effective anode thickness depend on r) will be assumed to be constant for simplicity. For low γ beams and thin titanium foil[6]

$$\theta_s \cong (20/\gamma)[d_a\ (\mathrm{cm})]^{1/2}, \tag{4}$$

where d_a is the anode foil thickness.

We assume a two-dimensional monoenergetic beam distribution function

$$f(\theta, p, r) = \frac{1}{\sqrt{\pi} p_0 \theta_s} \frac{\delta(p - p_0)}{\mathrm{erf}(\pi/\theta_s)} \exp\left[-\left(\frac{\theta - \theta_r}{\theta_s}\right)^2\right], \tag{5}$$

where p is the electron momentum, δ is the usual delta function, and erf is the error function. The corresponding beam fraction within the loss cone which can be adiabatically transmitted through the magnetic mirror is

$$R(r) \equiv \int_{-\theta_c}^{+\theta_c} d\theta \int_0^\infty dp\, p f(\theta, p, r)$$
$$= \{\mathrm{erf}[(\theta_c + \theta_r)/\theta_s] + \mathrm{erf}[(\theta_c - \theta_r)/\theta_s]\}[2\ \mathrm{erf}(\pi/\theta_s)]^{-1}, \tag{6}$$

where $\theta_c \equiv \sin^{-1}(1/M^{1/2})$ is the loss cone angle. The total adiabatic transmitted fraction is simply

$$T \equiv (2/r_b^2) \int_0^{r_b} dr\, r R(r)$$
$$= \left(\mathrm{erf}\left(\frac{\theta_c - \theta_b}{\theta_s}\right) + \mathrm{erf}\left(\frac{\theta_c + \theta_b}{\theta_s}\right) - \frac{\theta_c^2 + 0.5\theta_s^2}{\theta_b^2}\left[\mathrm{erf}\left(\frac{\theta_c - \theta_b}{\theta_s}\right) + \mathrm{erf}\left(\frac{\theta_c + \theta_b}{\theta_s}\right) - 2\ \mathrm{erf}\left(\frac{\theta_c}{\theta_s}\right)\right] - \frac{\theta_s}{\sqrt{\pi}\,\theta_b^2}\left\{(\theta_c - \theta_b) \times \exp\left[-\left(\frac{\theta_c + \theta_b}{\theta_s}\right)^2\right] + (\theta_c + \theta_b)\exp\left[-\left(\frac{\theta_c - \theta_b}{\theta_s}\right)^2\right]\right\}$$
$$+ \frac{2}{\sqrt{\pi}} \frac{\theta_s \theta_c}{\theta_b^2} \exp\left[-\left(\frac{\theta_c^2}{\theta_s^2}\right)\right]\Bigg)\left[2\ \mathrm{erf}\left(\frac{\pi}{\theta_s}\right)\right]^{-1}. \tag{7}$$

The analytic expression (7) gives almost identical results to the adiabatic numerical calculation by Freeman and Poukey.[1]

The adiabatically reflected beam electrons then turn back toward the diode, pass through the anode foil, bounce back from the cathode potential hill, and again pass through the anode. The mean squared angular scattering gained by the beam electrons by twice crossing the anode foil (thin titanium foil assumed) is roughly

$$\langle \delta\theta^2 \rangle \cong (400/\gamma^2) d_a\,(\mathrm{cm}) + 2\theta_r^2, \tag{8}$$

where the angular brackets denote the usual ensemble average. The first term in Eq. (8) is due to the thin foil scattering. The second term is due to the nonadiabatic crossings of the anode sheath. One may substitute Eq. (8) for the angular scattering, Eq. (4), to calculate the beam fraction which, after reflection, can now be adiabatically transmitted. However, we note that for many experiments the value of $\langle \delta\theta^2 \rangle$ in Eq. (8) is of the order of unity. In such cases, the reflected beam particles are roughly uniformly distributed in pitch angles. Hence, the fraction of beam scattered into the loss cone per reflection is simply $1 - \cos\theta_c$, which is the conical surface area in the loss cone divided by the total spherical surface area. The number of mirror reflections required for an average electron to be scattered into the loss cone is

$$N \cong (1 - \cos\theta_c)^{-1} \cong 2\theta_c^{-2}. \tag{9}$$

On the other hand, there is a radial scattering of the electron guiding center and it is related to the pitch-angle scattering by

$$\langle \delta r_i^2 \rangle \cong \rho^2 \langle \delta\theta^2 \rangle. \tag{10}$$

When an electron is scattered to a radius comparable to the cathode radius, it is no longer trapped by the diode electric field. The number of mirror reflections L required for an electron to be radially lost can be roughly defined by requiring the accumulative $\langle \delta r^2 \rangle$ to be equal to the square of the initial particle radial distance from the beam edge, i.e.,

$$\langle r_b - r \rangle^2 = \sum_{i=1}^{L} \langle \delta r_i^2 \rangle, \tag{11}$$

where r is the initial radial position of the electron. When $\langle \delta\theta^2 \rangle$ is of the order of unity (i.e., 90° scattering), Eq. (11) can be rewritten

$$L \cong (r_b - r)^2/\bar{\rho}_{cr}^2 \cong 2(r_b - r)^2/\rho_0^2 \tag{12}$$

by using Eq. (10), where $\bar{\rho}_{cr}$ is the average gyroradius of the electron. An electron will be scattered into the loss cone and transmitted through the mirror before it is radially scattered out of the beam channel if $L \geq N$, which is equivalent to

$$r/r_b \leq 1 - \rho_0/\sqrt{2}\, r_b (1 - \cos\theta_c)^{1/2} \tag{13}$$

from Eqs. (9) and (12). Equation (13) defines a core area at the anode in which all the electrons can eventually transmit through the mirror, while outside the core area only the adiabatic fraction [see Eq. (6)] will be transmitted. Transmission efficiency is enhanced over the adiabatic prediction in Eq. (7) only if the right-hand side of Eq. (13) is positive.

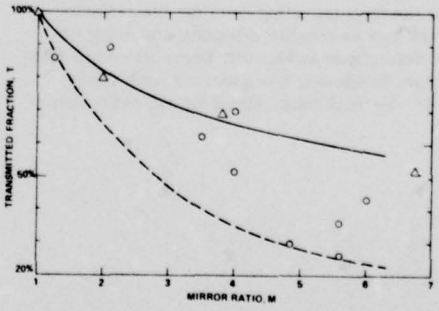

FIG. 2. Comparison between calculated transmission (solid curve) and data from Ref. 4 for various mirror ratios. The triangles and circles represent 20- and 100-cm transport data, respectively. The corresponding adiabatic transmission is also plotted (dashed curve) for comparison.

TABLE I. Comparison between calculated transmitted fraction (T_{cal}) with three experiments (T_{expt}).

References	1		2	3
I_b (kA)	70		40	400
γ	4.91		1.78	2.5
ν/γ	0.9		1.4	9.9
r_b (cm)	7.2		3.0	4.4
B_θ (kG)	1.94		2.67	18.2
B_z (kG)	2.5		4.0	9.0
M	3.7	6.7	3	4
T_{expt} (%)	69 ± 6	41 ± 5	83–96	75 ± 5
θ_b	0.66		0.59	1.1
θ_s	0.28		0.316	0.52
θ_c	0.547	0.40	0.65	0.524
T_{cal} (%)	65	40	83	70

We now proceed to compare the transmission calculation from Eqs. (6), (7), and (13) with several experiments, all satisfying the nonpinching criterion of Eq. (2). The experiments include those of Sandia Laboratories,[1] Cornell University,[2] and Physics International high[3] and low voltage.[4] Beam γ ranges from 1.78 to 4.91, ν/γ from 0.9 to 9.9, mirror ratios up to 6.7, B_z from 2.5 to 9 kG, and the observed transmitted fraction from 30% to 96%. We will calculate the transmitted fraction from Eq. (7) if the right-hand side of Eq. (13) is negative. Otherwise, the transmitted fraction will be the sum of the core area fraction from Eq. (13) and the adiabatic contribution outside the core, obtainable by integrating Eq. (6) from the core radius to r_b.

Figure 2 shows a comparison with data from Ref. 4, where transmitted fractions through 20- and 100-cm plasma channels are shown by triangles and circles, respectively, and the calculated results are shown as the solid curve. The calculation agrees well with the data of both 20- and 100-cm transport for mirror ratios less than 5. For $M=5-6$, the calculation deviates from the 100-cm transport data. This can be understood by noting that the total traveling time for the reflected beam, which can be roughly calculated by using the number of reflections in Eq. (9), becomes comparable with the beam lifetime (~100 nsec) for such cases (100 cm, $M=5-6$). Hence, electrostatic reflection in the diode must have been less than 100% efficient. Also shown in Fig. 2 as a dashed curve is the adiabatic transmission from Eq. (7). Except for large mirror ratio ($M=5-6$) and long plasma channel (100 cm), the adiabatic transmission alone cannot account for the observed transmission.

Table I shows a comparison with data from Refs. 1–3. Experimental beam and plasma parameters are shown at the top half of the table and results from the calculation are at the lower half. For Ref. 1, the transmission was entirely adiabatic [Eq. (7)] and agreement with the data is extremely good. For Ref. 3, one-third of the calculated transmission was adiabatic and two-thirds was due to enhancement; agreement with data is also good. For Ref. 2, adiabatic transmission and enhancement are about equal, and the calculation falls at the lower edge of the data range. The range (83–96%) was the result of various gas pressures (150–900 μ) in the guiding channel.

In summary, our model explains well the results of several experiments with wide ranges of beam parameters and transmission fractions. We acknowledge the presence of other potentially important mechanisms, such as formation of a virtual cathode[7] in cases of low transport chamber gas pressure, beam-plasma interactions which can contribute to beam transport losses, beam diamagnetic effects, and time variation of beam parameters. However, the good agreement of our calculation with the experiments strongly suggests that the mechanism we propose is often dominant in enhancing the beam transmission above the adiabatic prediction.

We would like to acknowledge helpful conversations with D. Dakin, C. Stallings, J. Benford, J. Shea, and K. Childers.

[1]P.E. Bolduc and E.L. Patterson, J. Appl. Phys. 43, 4006 (1972); J.R. Freeman and J.W. Poukey, *ibid.* 43, 4010 (1972).
[2]H. Davitian and J. Nation, Cornell University Report, 1973 (unpublished).
[3]P. Spence and K. Nielsen, Physics International Company, San Leandro, CA., 1975 (unpublished).
[4]C. Stallings, J. Benford, and K. Childers, Plasma Phys. 18, 317 (1976).
[5]D.A. Hammer, W.F. Oliphant, I.M. Vitkovitsky, and V. Fargo, J. Appl. Phys. 43, 5–8 (1972).
[6]For example, E. Fermi, *Nuclear Physics* (Univ. of Chicago Press, 1967).
[7]D.S. Prono, J.M. Creedon, I. Smith, and N. Bergstrom, J. Appl. Phys. 46, 3310 (1975).

DISTRIBUTION LIST

DEPARTMENT OF DEFENSE

Assistant to the Secretary of Defense
Atomic Energy
ATTN: ATSD (AE)

Director
Defense Advanced Rsch. Proj. Agency
ATTN: MISD/PM

Director
Defense Civil Preparedness Agency
Assistant Director for Research
ATTN: Admin. Officer

Defense Documentation Center
Cameron Station
12 cy ATTN: TC

Director
Defense Intelligence Agency
ATTN: DB-4C, E. O'Farrell
ATTN: DT-2
ATTN: DTICI, R. Rubenstein
ATTN: RSD-3A

Director
Defense Nuclear Agency
ATTN: RAEV
ATTN: TISI
3 cy ATTN: TITL
ATTN: DDST
2 cy ATTN: SPSS
ATTN: STVL

Commander
Field Command
Defense Nuclear Agency
ATTN: FCPR

Director
Interservice Nuclear Weapons School
ATTN: Document Control

Director
Joint Strat. Tgt. Planning Staff
ATTN: STINFO, Library
ATTN: JSAS

Chief
Livermore Division, Fld. Command, DNA
Lawrence Livermore Laboratory
ATTN: FCPRL

Commandant
NATO School (SHAPE)
ATTN: U.S. Documents Officer

Under Secretary of Defense for Rsch. & Engrg.
ATTN: S&SS (OS)

DEPARTMENT OF THE ARMY

Commander
BMD System Command
ATTN: BMDSC-TEN, N. Hurst
ATTN: SSC-TEN

DEPARTMENT OF THE ARMY (Continued)

Dep. Chief of Staff for Rsch., Dev. & Acq.
ATTN: DAMA-CSM-N
ATTN: DAMA-AOA-M

Chief of Engineers
2 cy ATTN: DAEN-RDM
ATTN: DAEN-MCE-D

Deputy Chief of Staff for Ops. & Plans
ATTN: MOCA-ADL
ATTN: Deputy Dir. of Nuclear Chem. Matters

Commander
Harry Diamond Laboratories
ATTN: DELHD-NP
ATTN: DELHD-RBA, J. Rosado
ATTN: P. Caldwell
ATTN: Scientific & Technical Info. Office

Commander
Redstone Scientific Information Ctr.
U.S. Army R&D Command
3 cy ATTN: Chief, Documents

Commander
U.S. Army Armament Material Readiness Command
ATTN: MA, Library

Director
U.S. Army Ballistic Research Labs.
ATTN: DRXBR-X, J. Meszaros
ATTN: DRDAR-BLE, W. Taylor
ATTN: DRDAR-BLE, J. Keefer
ATTN: E. Baicy

Commander
U.S. Army Communications Cmd.
ATTN: Tech. Ref. Div.

Commander
U.S. Army Engineer Center
ATTN: ATSEN-SY-L

Division Engineer
U.S. Army Engineer Div., Huntsville
ATTN: HNDED-SR

Division Engineer
U.S. Army Engineer Div., Ohio River
ATTN: ORDAS-L

Director
U.S. Army Engr. Waterways Exper. Sta.
2 cy ATTN: W. Flathau
ATTN: J. Strange
ATTN: L. Ingram
ATTN: Technical Library

Commander
U.S. Army Mat. & Mechanics Rsch. Ctr.
ATTN: Technical Library

Commander
U.S. Army Materiel Dev. & Readiness Cmd.
ATTN: Technical Library

DEPARTMENT OF THE ARMY (Continued)

Commander
U.S. Army Missile R&D Command
ATTN: DRCPM-PE-EA

Commander
U.S. Army Mobility Equip. R&D Ctr.
ATTN: DRDME-WC

Commander
U.S. Army Nuclear & Chemical Agency
ATTN: Library

Commander
U.S. Army Tank Automotive R&D Command
ATTN: DRDTA-UL

Commander
U.S. Army Test and Evaluation Comd.
ATTN: DRSTE-EL

DEPARTMENT OF THE NAVY

Chief of Naval Operations
ATTN: OP 981
ATTN: 604C4, R. Blaise

Chief of Naval Research
ATTN: Code 715

Officer-in-Charge
Civil Engineering Laboratory
Naval Construction Battalion Center
ATTN: R. Odello
ATTN: Code L08A

Commander
Naval Electronic Systems Command
Naval Electronic Systems Cmd. Hqs.
ATTN: Code 5032
ATTN: PME 117-21A

Commander
Naval Facilities Engineering Command
Headquarters
ATTN: Code 03A
ATTN: Code 09M22C

Commanding Officer
Naval Intelligence Support Ctr.
ATTN: NISC-45

Superintendent (Code 1424)
Naval Postgraduate School
ATTN: Code 2124

Director
Naval Research Laboratory
ATTN: Code 5410, J. Davis
ATTN: Code 2627
ATTN: Code 7701, J. Brown
ATTN: Code 7770, G. Cooperstein

Officer-in-Charge
Naval Surface Weapons Center
ATTN: Code WR43
ATTN: Code WA501

DEPARTMENT OF THE NAVY (Continued)

Commander
Naval Surface Weapons Center
Dahlgren Laboratory
ATTN: Technical Library & Information Services Branch

Commander
Naval Weapons Center
ATTN: Code 533

Commanding Officer
Naval Weapons Evaluation Facility
ATTN: Code 10
ATTN: R. Hughes

Director
Strategic Systems Project Office
ATTN: NSP-43

DEPARTMENT OF THE AIR FORCE

AF Geophysics Laboratory, AFSC
ATTN: LWW, K. Thompson
ATTN: SUOL, Rsch. Lib.

AF Institute of Technology, AU
ATTN: Library, AFIT Bldg. 640, Area B

AF Weapons Laboratory, AFSC
ATTN: DES-C, R. Henny
ATTN: DEP, J. Bratton
ATTN: DES-S, M. Plamondon
ATTN: DYC
ATTN: DYP
ATTN: NT
ATTN: SUL
ATTN: CA

Commander
Foreign Technology Division, AFSC
ATTN: NICD Library

Hq. USAF/RD
ATTN: RDQSM

SAMSO/DE
ATTN: DEB

SAMSO/DY
ATTN: DYS

SAMSO/IN
ATTN: IND, Maj D. Muskin

SAMSO/MN
ATTN: MNNH
ATTN: MMH

SAMSO/SK
ATTN: SKF, P. Stadler

Commander in Chief
Strategic Air Command
ATTN: NRI-STINFO, Library

DEPARTMENT OF ENERGY

Department of Energy
Albuquerque Operations Office
ATTN: Doc. Con. for Tech. Library

Department of Energy, Library, Rm. G-042
ATTN: Doc. Con. for Class. Tech. Lib.

Department of Energy
Nevada Operations Office
ATTN: Doc. Con. for Tech. Lib.

University of California
Lawrence Livermore Laboratory
ATTN: J. Nuckolls
ATTN: L-153
ATTN: L-18
ATTN: L. Woodruff
ATTN: Doc. Con. for Tech. Info. Dept. Lib.

Los Alamos Scientific Laboratory
ATTN: Doc. Con. for Reports Lib.

Sandia Laboratories
Livermore Laboratory
ATTN: Doc. Con. for Library & Security Classification Division

Sandia Laboratories
ATTN: Doc. Con. for L. Vortman
ATTN: Doc. Con. for 3141
ATTN: Doc. Con. for 5240, G. Yonas

DEPARTMENT OF DEFENSE CONTRACTORS

Aerospace Corp.
2 cy ATTN: Tech. Info. Services
ATTN: P. Mathur

Agbabian Associates
ATTN: M. Agbabian

Applied Theory, Inc.
2 cy ATTN: J. Trulio

Avco Research & Systems Group
ATTN: Research Lib.

Battelle Memorial Institute
ATTN: R. Klingsmith

BDM Corp.
ATTN: Corporate Library
ATTN: A. Lavagnino

BDM Corp.
ATTN: R. Hensley

Boeing Co.
ATTN: Aerospace Library
ATTN: R. Carlson

California Research & Technology, Inc.
ATTN: K. Kreyenhagen
ATTN: Technical Library

Dikewood Industries, Inc.
ATTN: L. Davis

EG&G Washington Analytical Services Center, Inc.
ATTN: Library

DEPARTMENT OF DEFENSE CONTRACTORS (Continued)

Ford Aerospace & Communications Corp.
ATTN: Tech. Info. Services

Ford Aerospace & Communications Corp.
ATTN: Technical Library
ATTN: MS G30, D. McMorrow

Gard, Inc.
ATTN: G. Neidhardt

General Electric Co.
Space Division
ATTN: J. Peden

General Electric Company-TEMPO
Center for Advanced Studies
ATTN: DASIAC

IIT Research Institute
ATTN: Documents Library

Institute for Defense Analyses
ATTN: IDA, Librarian

Ion Physics Corp.
ATTN: H. Milde

IRT Corp.
ATTN: R. Mertz

JAYCOR
ATTN: E. Wenaas

JAYCOR
ATTN: R. Sullivan

Kaman AviDyne
Division of Kaman Sciences Corp.
ATTN: Technical Library
ATTN: N. Hobbs
ATTN: E. Criscione

Kaman Sciences Corp.
ATTN: A. Bridges
ATTN: G. Butler, Jr.
ATTN: J. Hoffman
ATTN: W. Ware
ATTN: Library
ATTN: D. Bryce

Lockheed Missiles & Space Co., Inc.
ATTN: TIC-Library

Lockheed Missiles and Space Co., Inc.
ATTN: L. Chase

Martin Marietta Corp.
Orlando Division
ATTN: A. Cowan

Maxwell Laboratories, Inc.
ATTN: A. Miller
ATTN: P. Korn
ATTN: A. Kolb

McDonnell Douglas Corp.
ATTN: S. Schneider

Merritt CASES, Inc.
ATTN: J. Merritt

DEPARTMENT OF DEFENSE CONTRACTORS (Continued)

Mission Research Corp.
ATTN: C. Longmire
ATTN: W. Hart

Mission Research Corporation-San Diego
ATTN: V. Van Lint

Nathan M. Newmark Consulting Engineering Services
ATTN: N. Newmark

Northrop Corp.
Northrop Research and Technology Ctr.
ATTN: Library

Northrop Corp.
Electronic Division
ATTN: V. Demartino

Physics International Co.
ATTN: Doc. Con. for I. Smith
ATTN: Doc. Con. for S. Putnam
ATTN: Doc. Con. for C. Stallings
ATTN: Doc. Con. for L. Behrmann
ATTN: Doc. Con. for Tech. Lib.
ATTN: Doc. Con. for R. Swift
ATTN: Doc. Con. for B. Bernstein
ATTN: Doc. Con. for D. Orphal
ATTN: Doc. Con. for P. Spence
ATTN: Doc. Con. for F. Sauer
ATTN: Doc. Con. for B. Ecker
ATTN: Doc. Con. for V. Buck
ATTN: Doc. Con. for T. Young
ATTN: Doc. Con. for O. Lopez
ATTN: Doc. Con. for B. Chao

R & D Associates
ATTN: H. Brode
ATTN: C. Knowles
ATTN: W. Graham, Jr.
ATTN: R. Port
ATTN: W. Wright, Jr.
ATTN: L. Schlessinger
ATTN: C. Macdonald
ATTN: J. Lewis
ATTN: Tech. Info. Ctr.

DEPARTMENT OF DEFENSE CONTRACTORS (Continued)

Southwest Research Institute
ATTN: A. Wenzel

Spire Corp.
ATTN: R. Little

SRI International
ATTN: G. Abrahamson
ATTN: S. Ddairiki
ATTN: B. Gasten

R & D Associates
ATTN: H. Cooper

Systems, Science & Software, Inc.
ATTN: Library
ATTN: A. Wilson
ATTN: D. Grine
ATTN: T. Riney

Terra Tek, Inc.
ATTN: S. Green

Texas Tech University
ATTN: T. Simpson

TRW Defense & Space Sys. Group
ATTN: Tech. Info. Center
2 cy ATTN: P. Dai

TRW Defense & Space Sys. Group
San Bernardino Operations
ATTN: E. Wong

Vought Corporation
Michigan Plant
ATTN: Tech. Info. Center

Weidlinger Assoc., Consulting Engineers
ATTN: M. Baron

Weidlinger Assoc., Consulting Engineers
ATTN: J. Isenberg

Science Applications, Inc.
ATTN: J. Beyster
ATTN: Technical Library